



## Structure and thermal stability of zinc–nickel electrodeposits

C. BORIES, J.-P. BONINO\* and A. ROUSSET

Laboratoire de Chimie des Matériaux Inorganiques, ESA CNRS no. 5070, Université Paul Sabatier, 31062 Toulouse cedex, France

(\*author for correspondence, e-mail: bonino@iris.ups-tlse.fr)

Received 30 June 1998; accepted in revised form 5 January 1999

**Key words:** electrodeposition, structure, thermal stability, zinc–nickel

### Abstract

ZnNi alloys were electrodeposited from a chloride bath on steel substrates. The effect of nickel bath concentration on chemical composition, structure and microstructure of the deposits is demonstrated. From 0 to 13% nickel, the phases obtained do not correspond to that reported on the thermodynamic phase diagram. It is shown that the substitution of zinc by nickel is responsible for the formation of distorted  $\eta_d$  and  $\gamma_d$  phases corresponding to the supersaturated hexagonal  $\eta$  phase of zinc and to the unsaturated cubic  $\gamma$  phase of Zn–Ni alloy, respectively. Differential scanning calorimetry indicates that the thermal instability of the alloys containing up to 13 wt % of nickel, results from the crystallization of the  $\delta$  phase from the  $\eta_d$  and  $\gamma_d$  phases at around 200 °C and 250 °C, respectively.

### 1. Introduction

Zn–Ni alloy electrodeposits are of increasing interest as corrosion-resistant coatings for steel bodies. These coatings are more frequently used at room temperature but can be locally submitted to heat and any change in structure can lead to a change in susceptibility to corrosive atmospheres.

Although the optimum corrosion protection is obtained between 8 to 14 wt % nickel [1–4], the corresponding structure and microstructure required to provide maximum corrosion resistance by sacrificial behaviour is not well established because the structure of Zn–Ni electrodeposits is not accurately known in the limited domain of 0–14 wt % nickel. Whereas some authors [5–8] have reported that the phases in the Zn–Ni electrodeposits are in good agreement with the thermodynamic diagram, as for others [2, 4, 9–11] we have reported [12] that the phases contained in the Zn–Ni deposits on a rotating disc electrode do not correspond to those obtained at thermodynamic equilibrium. We proposed a phase diagram of electrodeposited Zn–Ni alloys in which, in contrast to the thermodynamic diagram, the  $\delta$  phase does not appear and the  $\eta$  and  $\gamma$  phases are supersaturated and unsaturated in nickel, respectively.

In an earlier paper [12] the codeposition of Zn and Ni on a rotating disc electrode (RDE) were described and were found to be controlled by their bath concentration when the rotation rate was higher than 1250 rpm. The nickel content of the deposits was the same as the  $\alpha$  ratio

in the electrolytic solution ( $\alpha = \text{Ni}^{2+}/\text{Zn}^{2+} + \text{Ni}^{2+}$ ). From Brenner's classification, this variation results from an equilibrium type codeposition process but can be changed with current density or stirring conditions. In this paper we present new investigations on the correlation between chemical composition, structure and microstructure of Zn–Ni deposits obtained in a cell set-up to represent an industrial surface finishing tank (i.e., with static vertical electrodes); also, we show, from thermal analysis, the effect of heat treatment on the structure of the Zn–Ni electrodeposits.

### 2. Experimental conditions

The apparatus used for electrodeposition consisted of a cell with static vertical electrodes (SVE) containing 600 cm<sup>3</sup> of electrolyte (Figure 1). Mechanical and air-flow agitation effected a high flow of solution at the electrode interfaces. The cathode was a low carbon steel sheet with a surface area of 60 cm<sup>2</sup> and the anode was an electrolytic nickel sheet with the same surface area. Before immersion, the steel surface was cleaned with hydrochloric acid (140 g dm<sup>-3</sup>) and rinsed with deionized water. The ZnNi alloy deposits were obtained at 60 °C from chloride-based electrolyte containing ZnCl<sub>2</sub> (334 g dm<sup>-3</sup>), NiCl<sub>2</sub>·6H<sub>2</sub>O (from 0 to 117 g dm<sup>-3</sup>) and KCl (350 g dm<sup>-3</sup>). To obtain Zn–Ni alloy deposits with varying nickel content, the nickel concentration of the electrolyte was varied from 0 to 14 wt %. The baths were prepared using deionized water and analytical

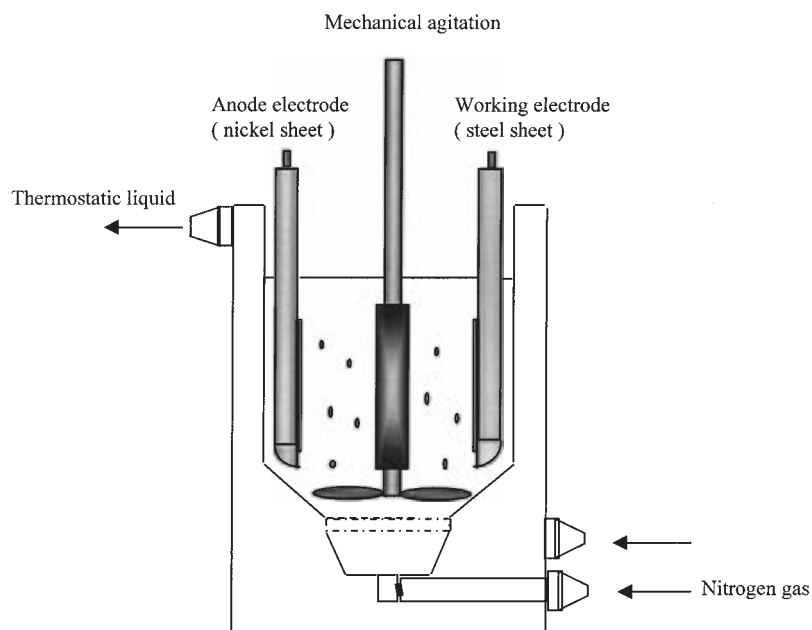


Fig. 1. Electroplating cell with static vertical electrodes (SVE cell).

grade chemicals. The electrolyte pH was adjusted to  $4.5 \pm 0.02$  with hydrochloric acid.

Electrodeposition was carried out under galvanostatic conditions at high current density ( $80 \text{ A dm}^{-2}$ ). After plating, the cathode was immediately washed with deionized water and air-dried. The thickness of each coating measured around  $10 \mu\text{m}$ .

The structure of as-deposited coatings was determined by X-ray diffraction with a Co anticathode ( $\lambda = 179.02 \text{ pm}$ ). After heat treatments at  $200^\circ\text{C}$  and  $300^\circ\text{C}$  phase identification was also performed from X-ray diffraction patterns. The morphology of as-deposited alloys was observed by scanning electron microscopy (SEM) with a Jeol apparatus and the chemical composition was determined by atomic absorption spectrometry.

The thermal stability was studied under argon by differential scanning calorimetry (DSC) with a heating rate of  $10^\circ\text{C min}^{-1}$ . To study the thermostructural evolution by X-ray diffraction, each sample was heated

under argon for 1 h at temperatures determined from the DSC curves.

### 3. Experimental results and discussion

#### 3.1. Chemical composition

Figure 2 shows the increase in nickel content of deposits obtained from the SVE cell against the  $\alpha$  ratio in solution. The composition reference line (CRL) corresponding to the alloy composition obtained in equilibrated codeposition conditions as defined by Brenner is plotted as a solid line. It can be seen that in the industrial stirring conditions chosen in these investigations, the nickel content in the deposits was slightly higher than in the electrolytic solution and the slope of the curve differed from the CRL characteristic of equilibrated codeposition of Zn and Ni. If we compare the increase in codeposited nickel with the slope of the

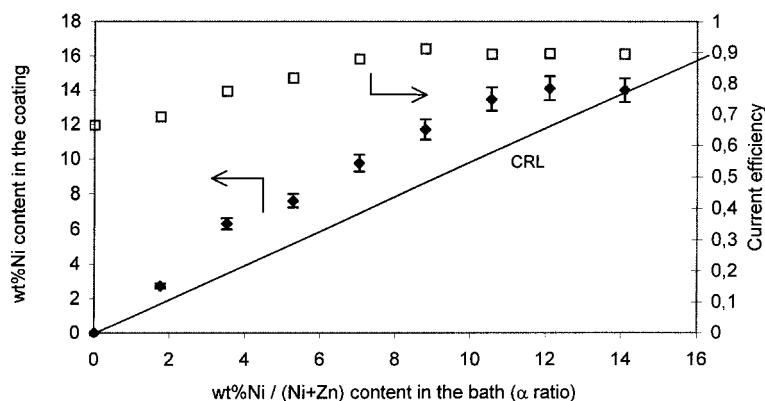


Fig. 2. Variation of nickel content in the coatings against the Ni/Ni + Zn ratio in the bath.

current efficiency curve, a similar inflexion in both beyond  $\alpha = 9$  wt % (12 wt % in deposits) is observed which shows a change in the reduction kinetics of metallic cations and protons which we have correlated with the change in microstructure and structure of the deposited alloys.

Before considering structural characterization by X-ray diffraction, we can see in Figure 3 that the evolution of the free corrosion potential against nickel content in deposits allows the alloys obtained between 0 and 17 wt % nickel to be separated into two families. In the first, below 12 wt % Ni, the free corrosion potential was around  $-1$  V vs SCE, while in the second, it increased up to  $-0.750$  V vs SCE. Some authors [4, 13, 14] have shown that the first value is characteristic of the potential of Zn dissolution from the hexagonal  $\eta$  phase of zinc, and the second characteristic of Zn dissolution from the cubic  $\gamma$  phase of Zn–Ni alloys. Although the values of free corrosion potential cannot be used to characterize the structure of deposits, they confirm that 12 wt % nickel in deposits is a critical value probably involving a change in the structure of the alloys.

### 3.2. Microstructure and structure

The microstructure of zinc alloy deposits, reported in Figure 4, clearly changes with the increase in quantity of nickel codeposited with the zinc. Pure zinc coatings (Figure 4(a)) were seen to be composed of agglomerates of platelets arranged with no apparent order. When a small quantity of nickel was introduced into the deposit,

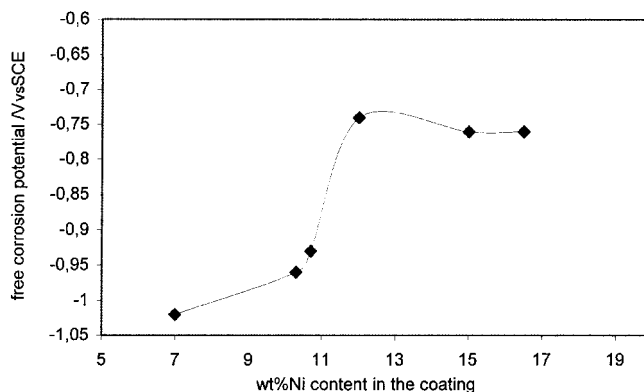


Fig. 3. Variation of free corrosion potential with against nickel content in the deposit.

grain refinement occurred through an alloying effect and the coatings were then made up of small agglomerated grains with a more isotropic shape (Figure 4(b)). Around 10 wt % nickel, submicrometre grains were well dispersed over the coating surface but their shape was not so well defined (Figure 4(c)). Increase in nickel content beyond 14 wt % involved a significant change in grain morphology. It can be seen in Figure 4(d) that the coatings with 15 wt % Ni are exclusively composed of cubic grains with pyramidal faces giving rise to grain growth with a preferential orientation. This very marked morphology probably results from an anisotropic growth rate of one crystallographic plane family of the cubic phase, which depends on the experimental conditions used. So, the microstructure changes with the

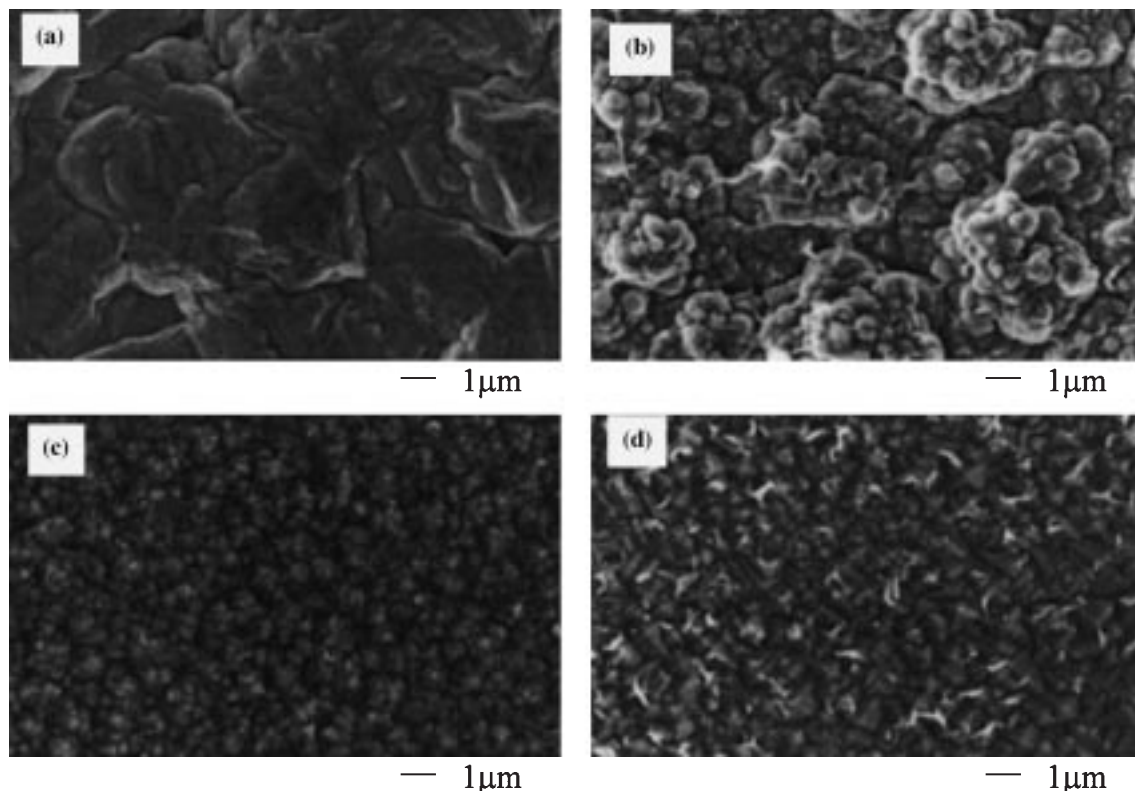


Fig. 4. Microstructure change of the coating against the nickel content in the deposits: (a) 0, (b) 6.5, (c) 10 and (d) 15 wt % Ni.

deposit nickel content; agglomerated platelets characteristic of pure electrodeposited zinc in the first range of compositions are gradually replaced by fine grains with pyramidal features in the second.

To explain this change in grain morphology we studied the structural variation of Zn–Ni alloys against nickel content in the coatings (Figure 5). The X-ray pattern of the pure Zn coating agrees exactly with the hcp structure of Zn (JCPDS card no. 4-831). As observed in the SEM study, the diffraction patterns show that the substitution of zinc atoms by a small quantity of nickel atoms involved a broadening of the diffraction peaks characteristic of grain refining. In addition to the peaks characteristic of Zn–Ni alloys, peaks related to the steel substrate appear. This confirms that substitution of zinc by 2.5 wt % nickel causes a shift of the  $\eta$  phase diffraction peaks. We had also observed a shift of the  $\eta$  phase diffraction peaks coatings obtained on a rotating disc electrode [12] which we explained by the growth of a distorted  $\eta_d$  phase by substitution of zinc by nickel atoms with a more isotropic electron cloud and lower atomic radius ( $r_{\text{Ni}} = 0.125$  nm,  $r_{\text{Zn}} = 0.137$  nm). Although the defor-

mation of the  $\eta$  phase has been confirmed for alloys containing more than 7.5 wt % nickel beyond this value the diffraction patterns show, as seen with the RDE cell, that the codeposited nickel contributed to the crystallization of body centred cubic (b.c.c.)  $\gamma$  phase (JCPDS card 6-653). Thus, beyond 6.5 wt % Ni, the deposits had two phases, the  $\gamma$  phase increased while the  $\eta$  phase gradually disappeared. However, owing to the superimposition of some diffraction peaks of  $\eta$  and  $\gamma$  phases, the limit of existence of the  $\eta$  phase could not be determined more precisely, but the free corrosion potential value of alloys, below 12 wt % nickel, around  $-1$  V vs SCE (Figure 3) suggests that the  $\eta$  phase is probably present in alloys up to 12 wt % nickel.

Thermodynamically, the Zn–Ni  $\gamma$  phase only appeared beyond 12.5 wt % nickel. Thus, electrodeposited alloys containing between 6.5 and 12.5 wt % Ni are therefore out of thermodynamic equilibrium. We evaluated, from two individual peaks of the  $\gamma$  phase, the (6 0 0) and (5 5 2) planes, the evolution of the  $a$  lattice parameter of the b.c.c. structure against the Ni content in alloys (Figure 6). The high value of the  $\gamma$  phase lattice parameter of the alloys containing below 7.5 wt % Ni

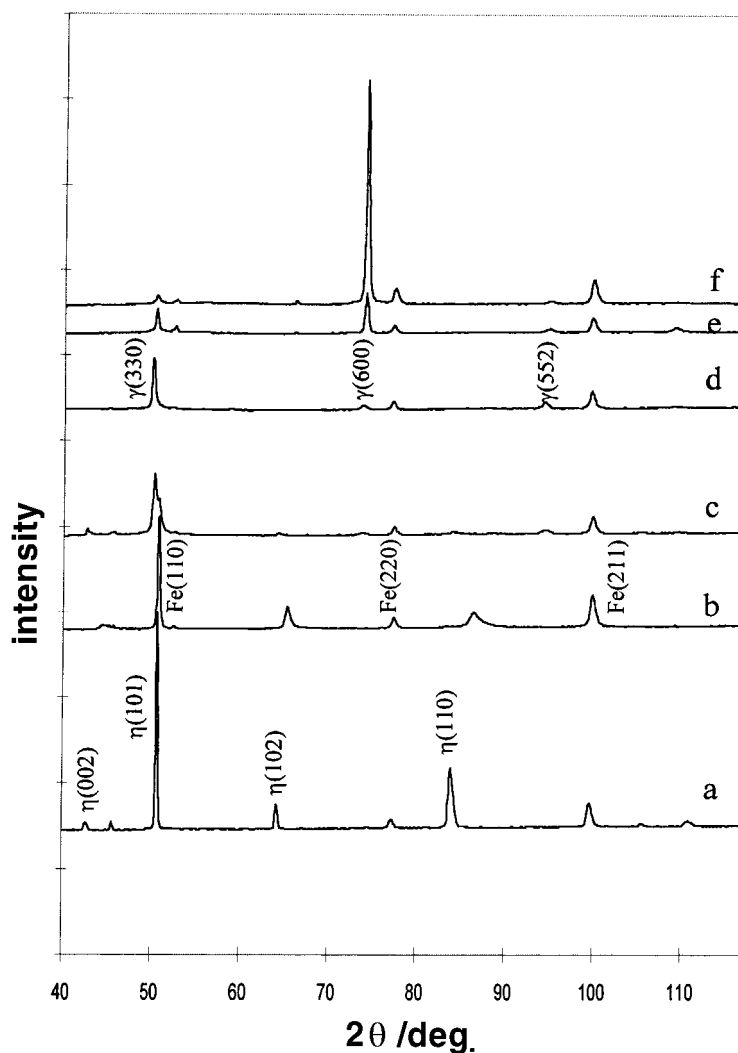


Fig. 5. X-ray diffraction patterns of the coating against the nickel content in the deposits: (a) 0, (b) 2.5, (c) 6.5, (d) 10, (e) 13.5 and (f) 15 wt % Ni.

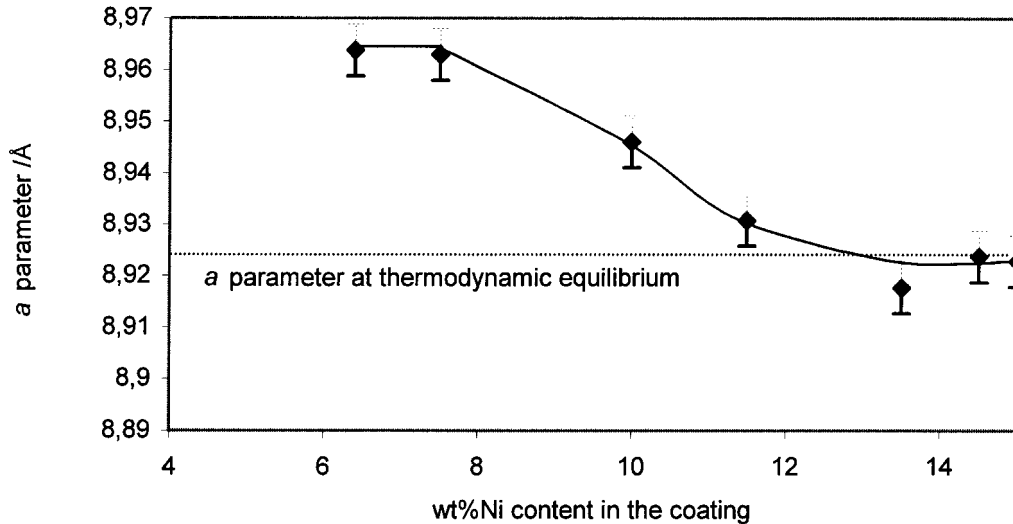


Fig. 6. Variation of  $a$  lattice parameters of the  $\gamma$  structure versus the nickel content in deposits.

shows that the cubic phase is distorted in this composition range. As already explained, the radius of the Zn atoms is greater than that of Ni, the supersaturation in Zn of the b.c.c. phase ( $\gamma_d$ ) explains its distortion and, consequently, the high value of the lattice parameter. When the Ni content in the deposits increased from 7.5 to 11.5 wt %, the lattice parameter decreased to the thermodynamic value. When this value is reached, X-ray diffraction patterns show a change in relative intensity of diffraction peaks (3 3 0) and (6 0 0). If we consider that, in the  $\theta$ - $2\theta$  X-ray diffraction method, only the planes parallel to the sample surface diffract, the high intensity of (3 3 0) planes in the supersaturated cubic phase, shows that the grains orientated with (3 3 0) planes parallel to the coating are the most abundant in the coatings. From 13 wt % Ni, a change in preferential orientation appears and the grains are preferentially orientated with (6 0 0) planes parallel to the coating surface. As can be seen for the coating with 15 wt % Ni, this phenomenon increases with the supersaturation of the  $\gamma$  phase and the lattice parameter decreases. Thus, the pyramidal features of the grains already observed by SEM can be explained by the preferential orientation of grains resulting from the greater reactivity of the (1 1 1) plane during the growth of the b.c.c. phase.

From these results an electrodeposited phase diagram for Zn–Ni alloys can be defined: this is compared in

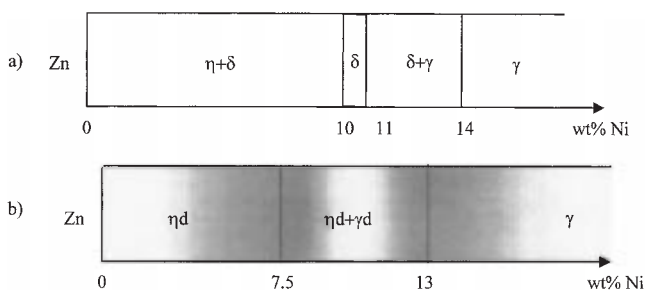


Fig. 7. Zinc–nickel phase diagrams at thermodynamic equilibrium (a) and electrodeposited (b).

Figure 7 to the thermodynamic diagram. The X-ray diffraction data of the  $\delta$  phase, presented in the thermodynamic phase diagram reported in the literature [15], does not allow its identification in electrodeposited alloys. Although the limits of existence of the hexagonal phase were not clearly defined from X-ray diffraction, the free corrosion potential of alloys seem confirm that the  $\eta$  phase is present in alloys up to 12 wt % nickel. Thus, the SVE cell confirms the RDE cell findings. The  $\delta$  phase is replaced by distorted  $\eta_d$  and  $\gamma_d$  phases and both phases are present in alloys over a composition range between 6.5 and 12 wt% nickel.

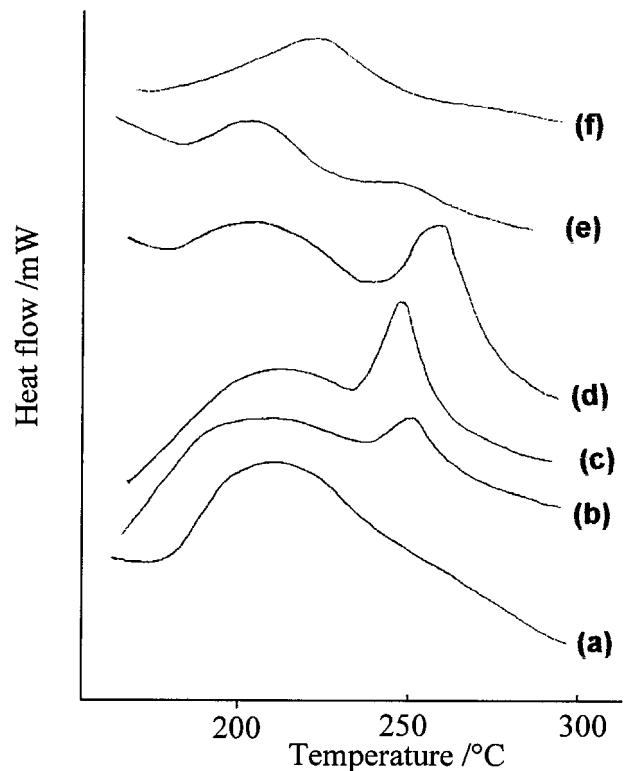


Fig. 8. Thermograms of the zinc–nickel coatings obtained from DSC: (a) 0, (b) 2.5, (c) 6.5, (d) 10, (e) 13.5 and (f) 15 wt % Ni.

To confirm the presence of distorted  $\eta_d$  and  $\gamma_d$  phases and the out-of-equilibrium state of the electrodeposited alloys containing between 6.5 and 13 wt % of nickel, we studied their thermal stability by DSC analyses and X-ray diffraction after annealing.

### 3.3. Thermal stability

DSC analysis was carried out in the temperature range 25 to 300 °C. The alloys selected for this study contained between 2.5 and 15 wt % nickel. The thermograms

(Figure 8) show that all the electrodeposited alloys present a wide exothermic peak at low temperature from 150 °C, with a maximum reaction heat around 200 °C. For the alloys containing between 2.5 and 13 wt % Ni, a second exothermic reaction, more distinct than the first one, appears at around 230 °C.

No noticeable structural modifications of the alloys containing less than 6.5 wt % Ni were observed and for this reason Figure 9 only shows the X-ray diffraction patterns of the three characteristic alloys containing 7.5, 10 and 13.5 wt % nickel, annealed at 200 and 300 °C for

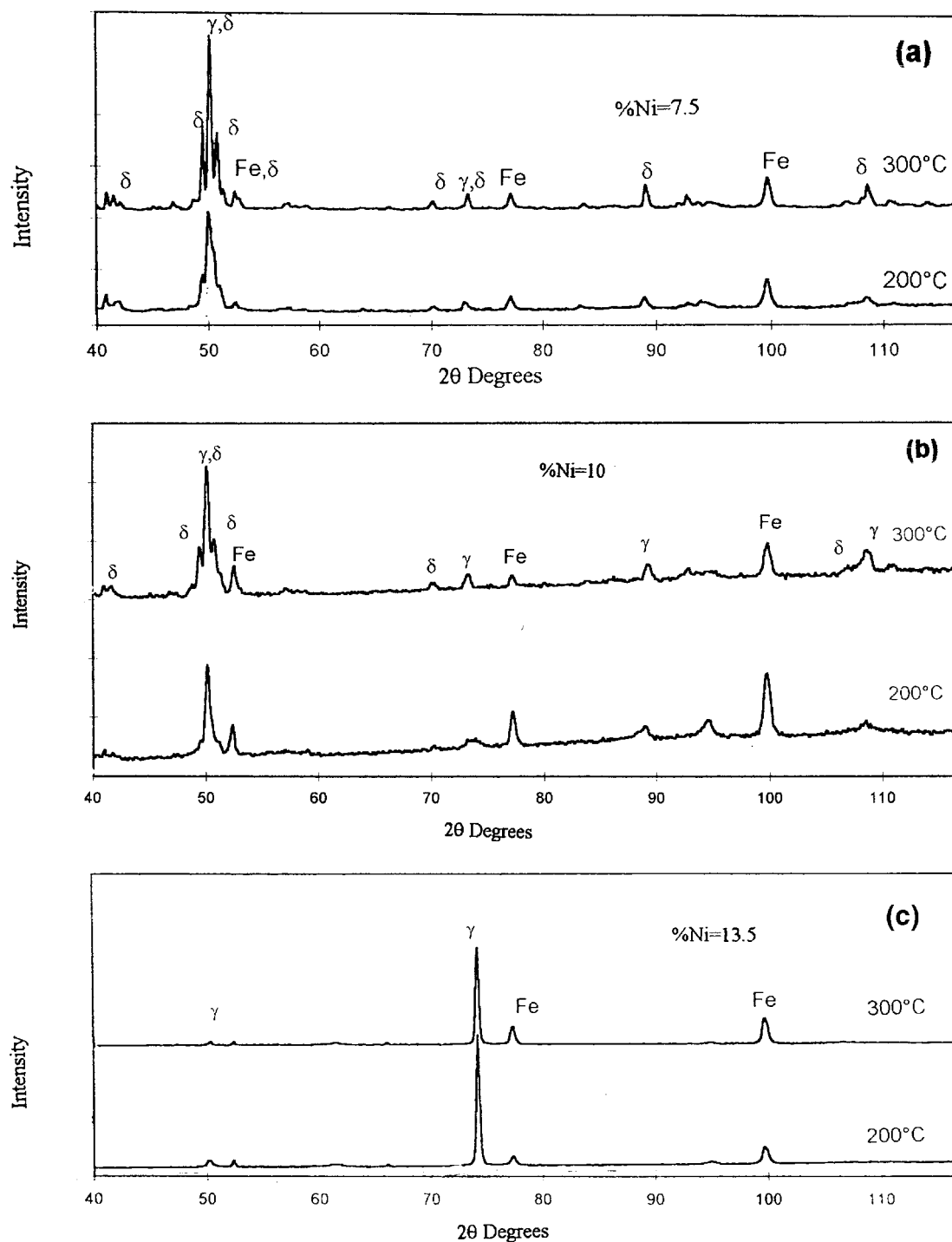


Fig. 9. Structural changes after annealing at different temperatures of zinc–nickel coatings: (a) 7.5, (b) 10 and (c) 13.5 wt % Ni.

one hour. It can be seen that the alloys containing more than 7.5 wt % undergo a structural transformation from 200 °C which corresponds to the precipitation of a new phase, different to  $\eta$  and  $\gamma$ , for which the diffraction peaks correspond to the monoclinic  $\delta$  phase reported by Bardin [15]. When the alloys are annealed at the temperature corresponding to the second exothermic peak, the  $\delta$  phase is clearly identifiable in the diffraction patterns. Thus, the second step of crystallization, results from the transformation of the unstable  $\gamma_d$  phase into the  $\gamma$  and  $\delta$  phases. For the single-phase  $\gamma$  alloys, the exothermic peak at 250 °C disappears and the annealing treatment at 300 °C does not modify the diffraction patterns.

#### 4. Conclusion

The structure of Zn–Ni coatings obtained from static vertical electrodes (SVE cell) did not differ from the structure of alloys obtained in controlled hydrodynamic conditions (RDE cell). We confirmed that the phase diagram of electrodeposited Zn–Ni alloys is different from the thermodynamic diagram. The  $\delta$  phase is replaced by distorted  $\eta_d$  and  $\gamma_d$ . We showed by thermal analysis, that the electrodeposited alloys containing up to 13 wt % nickel were out-of-equilibrium. The first transformation, at 200 °C, corresponds to the crystallization of  $\delta$  and  $\eta$  phases from the supersaturated hexagonal phase  $\eta_d$ , then the second transformation, around 250 °C, corresponds to the precipitation of  $\delta$  and  $\gamma$  phases from the unsaturated cubic phase  $\gamma_d$ . These

results show the thermal instability of electrodeposited Zn–Ni alloys with less than 13% nickel which may limit their application in corrosion protection of thermally selected bodies.

#### References

1. H.L. Harvie, In: J. Krauss and D.K. Matlock (eds) *Zn-Based Steel Coating Systems: Metallurgy and Performance*, The mineral, Metals and Materials Society, (1990) pp. 157–169.
2. M.R. Lambert, R.G. Hart and H.E. Townsend, SAE paper 831817, (1983) 1153.
3. M.F. Mathias, C.M. Villa and T.W. Chapman, *J. Appl. Electrochem.* **20** (1990) 1.
4. A. Shibuya, T. Kurimoto and M. Kimoto, The Sumitomo search, **31** (1985) 75.
5. L. Felloni, R. Fratesi, E. Quadrini and G. Roventi, *J. Appl. Electrochem.* **17** (1987) 574.
6. R. Fratesi and G. Roventi, *J. Appl. Electrochem.* **22** (1992) 657.
7. Y.L. Chen and D.D. Snyder, In: J. Krauss and D.K. Matlock (eds) *Zn-Based Steel Coating Systems: Metallurgy and Performance*, (1990) pp. 95–107.
8. I. Nenov, I. Gadshov and K. Pangarov, *Galvanotechnik* **75** (1984) 1107.
9. A. Seki and K. Kamei, *I.S.I.J. International* **32** (1992) 1306.
10. Y. Ohmori, K. Kondo, K. Kamei and S. Hinotani, *Mater. Res. Soc. Symp. Proc.* **122** (1988) 553.
11. K. Kondo, *Tetsu to Hagane* **77** (1991) 886.
12. S. Bruet-Hotellaz, J-P. Bonino and A. Rousset, *J. Mater. Sci.*, in press. (1998)
13. K.R. Baldwin, M.J. Robinson and C.J.E. Smith, *Corros. Sci.* **36** (1994) 1115.
14. S. Bruet Hotellaz, PhD thesis, Université Toulouse III France, (1996)
15. O. Bardin, PhD thesis, Institut National Polytechnique, Toulouse, France (1995).